International Journal of Multiphase Flow 144 (2021) 103787

Contents lists available at ScienceDirect

International Journal of Multiphase Flow

journal homepage: www.elsevier.com/locate/ijmulflow

Coalescence of fluid particles with deformable interfaces in non-Newtonian media

Maria Fanebust, Suat Canberk Ozan *, Hugo Atle Jakobsen

Department of Chemical Engineering, Norwegian University of Science and Technology (NTNU), N- 7491 Trondheim, Norway

ARTICLE INFO

Keywords:
Coalescence
Non-Newtonian
Film drainage
Coalescence time
Shear-thinning
Shear-thickening

ABSTRACT

The drainage of the non-Newtonian film between two approaching fluid particles are studied. The non-Newtonian continuous phase is a generalized Newtonian fluid that obeys the power-law model, and the deformable particle interfaces are allowed to have any degree of tangential mobility. The interaction is a gentle collision with a constant relative approach velocity. The film equations are simplified by using the lubrication theory in the thin film limit and combined with the boundary integral method. The effect of the non-Newtonian behavior on the film drainage and on the coalescence time is investigated through the power index. It is found that the non-Newtonian behavior significantly affects the number and type of the rims emerging at the interfaces. At a given approach velocity, when there are no rims or when the interfaces are fully mobile, the coalescence times for Newtonian and non-Newtonian fluids appear to be the same. Otherwise, the coalescence time increases with the power index, i.e., it is faster for shear-thinning fluids and slower for shear-thickening ones. This effect of the non-Newtonian behavior is found to amplify with the tangential mobility of the interfaces and the relative approach velocity.

1. Introduction

The coalescence of fluid particles plays a crucial role in several industrial fields such as cosmetics, food, pharmaceuticals, and petrochemical industries, where dispersed flows are commonly encountered. Within these industries, chemical and biochemical reactors are frequently employed. In many processes, the continuous phase is a Newtonian one; however, non-Newtonian fluids, for instance, polymer solutions, crude oil, or biofluids, are also encountered. The rheological complexity of the continuous phase may influence the interactions between the fluid particles and heat and mass transfer in the unit, influencing the coalescence process and playing a critical role in the reactor performance. The detailed impact of fluids' complex rheological properties on coalescence is not yet fully understood. Thus, to better understand this concept, the single event of coalescence between two fluid particles in a non-Newtonian continuous medium should be studied.

To describe the coalescence progression, the following steps are suggested based on the observations of Shinnar and Church (1960):

1. The external flow brings the fluid particles close enough for them to interact
2. A thin film of the continuous phase is entrapped between the particles
3. The film drains until reaching a critical film thickness value
4. The film ruptures, and coalescence occurs as longs as the contact time of the particles is longer than the time needed to reach the critical film thickness value

Although these steps have been proposed through observations on a Newtonian system, the same mechanisms can be expected to apply to the systems involving non-Newtonian fluids.

Coulaloglou (1975) gives a statistical method for estimating the coalescence efficiency, λ_c, based on the film drainage approach:

$$\lambda_c = exp\left(-\frac{t_{drainage}}{t_{contact}}\right) \tag{1}$$

This model is restricted to gentle collisions, in which the radius of the particle is significantly larger than the radius of the emerging thin film. The drainage time is then estimated through hydrodynamic modeling of the film drainage. A great number of film drainage models which are built by considering various levels of complexity exist in the literature for the Newtonian systems. A comprehensive overview of these studies can be found in Chesters (1991) and Liao and Lucas (2010). As the film between the particles is fairly thin, the lubrication theory is often applied to simplify the hydrodynamic models. Furthermore, the film drainage models are commonly categorized based on the particle interface's deformability, and tangential mobility (Chesters,

* Corresponding author.
E-mail address: canberk.ozan@ntnu.no (S.C. Ozan).

https://doi.org/10.1016/j.ijmultiphaseflow.2021.103787
Received 1 June 2021; Received in revised form 27 July 2021; Accepted 5 August 2021
Available online 11 August 2021
0301-9322/© 2021 The Authors. Published by Elsevier Ltd. This is an open access article under the CC BY license (http://creativecommons.org/licenses/by/4.0/).

1991). The former categorization separates models with rigid spherical (or spherical cap-shaped) fluid particles and the particles with deformable interfaces, which can model the experimentally observed dimple formation (Derjaguin and Kussakov, 1939). Moreover, the interfaces of the particles are either immobile, partially mobile, or fully mobile. When the interfaces are immobile, the film drainage is governed by the viscous forces, which results in a parabolic velocity profile in the film. The complete immobilization of the interface may stem from a significantly viscous dispersed phase (Bazhlekov et al., 2000) or from surfactant presence, which creates Marangoni stresses at the interface and also gives the interface viscous or viscoelastic properties (Ozan and Jakobsen, 2019b, 2020). When the tangential mobility of the interface completely controls the drainage, the velocity profile in the film resembles a plug-flow, and the interfaces are said to be fully-mobile. In this case, the parabolic component of the velocity profile is insignificant. When neither the plug nor the parabolic profiles are negligible, the interfaces are described as partially-mobile. Here immobilizing factors, i.e., high dispersed phase viscosity and the surfactant presence, play a key role in determining the extent of the tangential mobility of the interfaces.

The boundary integral theory can be employed to determine the tangential velocity of the interface (Davis et al., 1989). This method permits the coupling of the dispersed and the continuous phase velocity fields through the stress balances and the no-slip condition without requiring the solution of the internal flow in the particles, thereby considerably reducing the computational costs. Following Davis et al. (1989), the use of the boundary integral method has been established as a standard procedure in the literature and applied in many Newtonian film drainage studies where the interfaces are fully or partially mobile (Yiantsios and Davis, 1991; Abid and Chesters, 1994; Klaseboer et al., 2000; Bazhlekov et al., 2000; Ozan and Jakobsen, 2019a; Ozan et al., 2021). Yiantsios and Davis (1991) investigated the interactions between two fluid particles with deformable interfaces and found that coalescence was not possible without attractive van der Waals forces. In addition, they revealed that for strong van der Waals forces, the film rupture occurs at the center, which they call a nose rupture. As the van der Waals forces weaken, the capillary forces are allowed to act first and cause the formation of the rims at the interface. The films then eventually rupture from the rims, i.e., rim rupture is seen. Abid and Chesters (1994) considered the centerline, constant approach velocity collisions in the presence of the attractive intermolecular forces by considering fully mobile interfaces and proposed a critical film thickness expression, below which the film ruptures. Klaseboer et al. (2000) investigated the film drainage with two different theoretical models: one where the interfaces are immobile, i.e., the velocity profile is parabolic, and one with fully mobile interfaces meaning the velocity profile only has a plug flow contribution. Klaseboer et al. (2000) also gathered experimental data by analyzing the constant velocity droplet interactions and concluded that the immobile model represented the experimental results better. Bazhlekov et al. (2000) established a model suitable for all ranges of mobility, whose effect appears through the dispersed to continuous phase viscosity ratio in the thinning equation. They considered both constant velocity and constant interaction force collisions and showed the immobilizing effect of the dispersed phase viscosity on the interfaces. Via a similar model, Ozan and Jakobsen (2019a) presented the coalescence time as a function of the relative approach velocity and the viscosity ratio by also taking the attractive van der Waals forces into account. They identified three successive regimes with increasing approach velocity. First, in the low-velocity drainage regime, the coalescence time decreases with increasing approach velocity following a power-law type relation. In this regime, nose rupture occurs. Then, the dimple formation starts in the second regime, and the rupture location switches to the rim. Here, the coalescence time still decreases with the velocity but less and less dramatically. As the last regime is reached, the coalescence time exhibits a minimum and starts increasing, which coincides with the emergence of secondary rim structures at the interface. In a recent study, Ozan et al. (2021) incorporated a force balance to the film drainage model to represent the time-dependent behavior of the approach velocity instead of assuming a constant velocity or a constant interaction force. This force balance included the buoyancy and the drag forces, as well as the added mass effects and the resistance of the film to the drainage. The resistance was found to be capable of slowing down the approach considerably and even reverse the process to result in the particles to rebound instead of coalesce.

On the other hand, far less research is dedicated to coalescence within non-Newtonian continuous media in the literature, most of which focused on the factors influencing in-line coalescence of rising bubbles. Acharya et al. (1978) reported through experimental observations that the elasticity in the continuous phase tends to hinder film drainage and thereby delay coalescence. Dekee et al. (1986) investigated experimentally the effect of the bubble wake and the approach velocity on the bubble coalescence features within a vertical arrangement in purely shear-thinning and viscoelastic polymer solutions. In several works, Li and coworkers (Li et al., 1997; Li, 1999; Li et al., 2001) studied the interactions and the coalescence of rising bubbles in non-Newtonian fluids. Some of their key findings were that the stress created by the passage of bubbles and their relaxation due to the fluid's memory are central to bubble interactions and coalescence. Lin and Lin (2009) reported that the drag force and pushing force cause acceleration of the trailing bubble to the leading one. Al-Matroushi and Borhan (2009) found that the flow disturbance behind the leading bubble and the viscoelastic nature of the continuous phase appear to hinder bubble coalescence. Sun et al. (2017) investigated the effects of operation conditions on bubble minimum in-line coalescence height in non-Newtonian fluid described by the power-law. Zhu et al. (2018) studied the velocity evolution for the coalescence of two in-line bubbles rising in non-Newtonian fluids experimentally and also developed a theoretical model based on Newton's second law. Although these studies offer much in understanding the overall coalescence behavior in a column, they do not provide precise control over some key parameters, such as the approach velocity, which makes it near impossible to isolate the effects of these parameters from others. The experiments studying the so-called parallel bubbles' growth, e.g. Fan et al. (2020), enable the investigation of the effect of the approach velocity. Furthermore, in such experiments, as the velocity can be fixed to a precisely-controlled value, it is possible to examine the impact of other parameters, e.g., the rheological properties, on the coalescence without the interference of the changes and fluctuations in the velocity itself. In contrast to the in-line studies, there have been far fewer looking into the coalescence process of parallel bubbles growing side-by-side in non-Newtonian fluids. Fan et al. (2020) investigated the coalescence dynamics of twin bubbles growing from two adjacent nozzles in CMC-solutions described by the power-law. They concluded that for high enough gas flow, the coalescence efficiency increases with the CMC concentration, i.e., the coalescence time is lower when the solution is more shear-thinning.

In the current work, the film drainage behavior and the coalescence time for fluid particles in non-Newtonian media are investigated by employing a hydrodynamic film drainage model. The non-Newtonian film is assumed to follow the power-law, and the interfaces are modeled as deformable ones that are allowed to be of any degree of tangential mobility.

The article outlines the following: The mathematical model employed and the physical configuration are presented in Section 2. A description of the numerical procedure and its validation are given in Section 3.1. Section 3.2. presents the results consisting of the film drainage behavior and the coalescence time, together with their discussion. Finally, the conclusions derived throughout the study are summarized in Section 4.

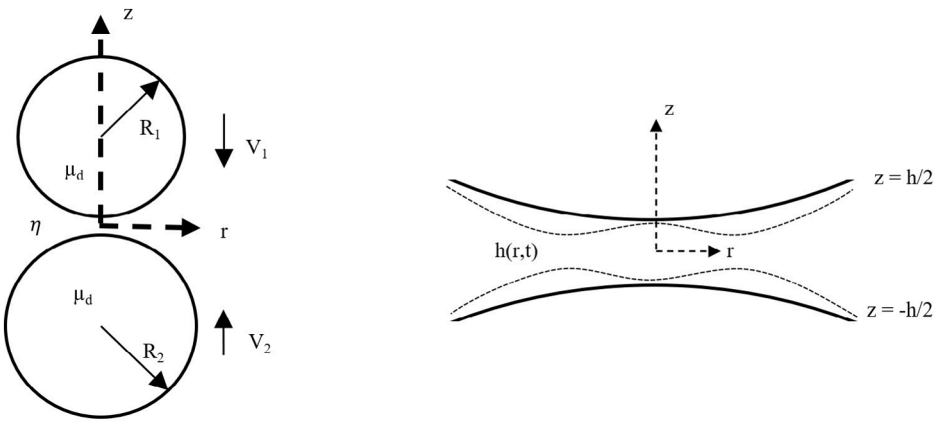

Fig. 1. Physical system consisting of two approaching fluid particles in non-Newtonian medium with viscosity η, and the thin deformable film entrapped by them.

2. Theory

This work studies the axisymmetrical interactions between two fluid particles in non-Newtonian continuous media. The physical configuration is depicted in Fig. 1. The particles are considered to approach each other with constant relative approach velocity, $V_{app} = V_2 - V_1$, along their center lines. Moreover, the particles are allowed to have different radii, i.e., R_1 is not necessarily equal to R_2, as marked in Fig. 1. The particles entrap a thin film of the non-Newtonian continuous phase, whose viscosity η follows the power-law model. This film eventually starts to drain and has a thickness, $h = h(r,t)$. The flow is assumed to be incompressible, while the interfaces between the continuous and the dispersed phases are modeled as deformable surfaces, and the surface tension, σ, is constant. Furthermore, it is assumed that the particles collide gently, such that both particles' radii are much larger than the radius of the entrapped film. Consequently, the equivalent radius , R_p defined by Abid and Chesters (1994):

$$\frac{1}{R_p} = \frac{1}{2}\left(\frac{1}{R_1} + \frac{1}{R_2}\right), \tag{2}$$

can be used to describe both particle sizes. Then it is possible to model the collision between unequal-sized particles as the collision of equal-sized ones with a radius of R_p. Hence, the system becomes symmetric around the radial axis. Then, the thin film sketch in Fig. 1 can be divided into four equal quadrants, where it is only necessary to obtain the solution for one of them. The quadrant with $r \geq 0$ and $z \geq 0$, where the interface can be described by $z = h/2$, is chosen. Furthermore, the film is described in cylindrical coordinates, and the particle interfaces are allowed to deform under the collision.

2.1. Governing equations and interface conditions

Due to the assumption of a thin film, the lubrication theory is applied. The relation between characteristic scales of film thickness, $\bar{h}$, and the radial coordinate, $\bar{r}$, is given as:

$$\frac{\bar{h}}{\bar{r}} = \epsilon \ll 1. \tag{3}$$

In addition, for a gentle collision, $\bar{h}$ and $\bar{r}$ can be expressed in terms of the equivalent particle radius (Ozan and Jakobsen, 2019a):

$$\bar{h} = \epsilon^2 R_p, \qquad \bar{r} = \epsilon R_p \tag{4}$$

Notice that initially the thin film and the gentle collision assumptions yield two different small parameters. However, for the particular configuration studied here, it is possible to manipulate these small parameters to end up with a single ϵ as described in Eqs. (3)–(6) of Ozan and Jakobsen (2019a).

The continuity equation and the equation of motion govern the film flow. Here, the dominant terms in the equations are given directly in the thin film limit without discussing the order of magnitude of each term, as the simplification process and the resulting sets of equations are well-established in the literature, e.g., by Chan et al. (2011). The dominant terms are the same as the Newtonian case, except for the non-constant viscosity η. Then, in the thin film limit, the governing equations read

$$\frac{1}{r}\frac{\partial}{\partial r}(r v_r) + \frac{\partial v_z}{\partial z} = 0 \tag{5}$$

and

$$\frac{\partial P}{\partial r} = \frac{\partial}{\partial z}\left(\eta \frac{\partial v_r}{\partial z}\right), \qquad \frac{\partial P}{\partial z} = 0 \tag{6}$$

where v_r and v_z denote the r and z components of the velocity, and P is the excess pressure in the film. Note that the θ-component of the equation of motion is not required due to the axisymmetry. Furthermore, η is the non-Newtonian viscosity obeying the power-law:

$$\eta = m\dot{\gamma}^{n-1} = m\left|\frac{\partial v_r}{\partial z}\right|^{n-1} \tag{7}$$

Here, m is the flow consistency index, n is the power index and $\dot{\gamma}$ is the magnitude of the rate of deformation tensor, $\dot{\gamma} = \nabla \mathbf{v} + (\nabla \mathbf{v})^{\mathrm{T}}$, where $\mathbf{v}$ is the velocity vector in the film. Note that originally the magnitude $\dot{\gamma}$ includes other velocity components as well, but in the thin film limit these components are negligible compared to $\frac{\partial v_r}{\partial z}$. The power-law is further inserted into the equation of motion, which yields:

$$\frac{\partial P}{\partial r} = \frac{\partial}{\partial z}\left(m\left|\frac{\partial v_r}{\partial z}\right|^{n-1}\frac{\partial v_r}{\partial z}\right), \qquad \frac{\partial P}{\partial z} = 0 \tag{8}$$

Since the model is only solved for the $r \geq 0$, $z \geq 0$ quadrant, where v_r decreases with z, the velocity gradient in the viscosity model is negative. As also m is a constant, then, Eq. (8) is rewritten as:

$$\frac{\partial P}{\partial r} = -m\frac{\partial}{\partial z}\left[\left(-\frac{\partial v_r}{\partial z}\right)^n\right] \tag{9}$$

The continuous and the dispersed phase flows are coupled via boundary conditions valid at the interface, $z = h/2$: the no-slip condition, the kinematic condition, and the normal and the tangential components of the stress balance. In the thin film limit, these conditions respectively yield:

$$v_r = U_t, \tag{10}$$

$$v_z - \frac{1}{2}\frac{\partial h}{\partial r}v_r = \frac{1}{2}\frac{\partial h}{\partial t}, \tag{11}$$

$$P = \frac{2\sigma}{R_p} - \frac{1}{2r}\frac{\partial}{\partial r}\left(r\frac{\partial h}{\partial r}\right), \tag{12}$$

and

$$-\eta\frac{\partial v_r}{\partial z}=\tau_d, \tag{13}$$

where U_t is the tangential velocity of the interface, σ is the surface tension and τ_d is the particle side tangential stress evaluated at the interface. Due to the assumption of gentle collision, the particle side pressure deviations are neglected in Eq. (12). Moreover, at a considerable radial distance, r_∞, it is presumed that the shape of the interface and the approach velocity are unaffected by the collision. Thus, the following boundary conditions hold:

$$\frac{\partial h}{\partial t}\Big|_{r_\infty}=-V_{app}, \tag{14}$$

and

$$P|_{r_\infty}=0. \tag{15}$$

Whereas the axisymmetry implies:

$$\frac{\partial h}{\partial r}\Big|_{r=0}=0, \tag{16}$$

and

$$\frac{\partial P}{\partial r}\Big|_{r=0}=0, \tag{17}$$

The initial film thickness is described as:

$$h=h_{00}+\frac{r^2}{R_p} \tag{18}$$

to resemble the curvature of a sphere.

Moreover, following Davis et al. (1989), the boundary integral of the Stokes flow is employed to calculate the tangential velocity of the interface:

$$U_t=\frac{1}{\mu_d}\int_0^{r_\infty}\phi\ \tau_d\,\mathrm{d}\rho, \tag{19}$$

where

$$\phi=\frac{1}{2\pi}\rho\int_0^{\pi}\frac{\cos\theta}{\sqrt{r^2+\rho^2-2r\rho\cos\theta}}\,\mathrm{d}\theta \tag{20}$$

2.2. Dimensionless equations

Based on the relationship between the characteristic film thickness and radius scales, as shown in Eq. (3), the following transformations:

$$r=\epsilon R_p\tilde{r},\quad h=\epsilon^2R_p\tilde{h},\quad P=\frac{\sigma}{R_p}\tilde{P},\quad v_r=\frac{\epsilon^3\sigma}{\eta_0}\tilde{v}_r,$$
$$v_z=\frac{\epsilon^4\sigma}{\eta_0}\tilde{v}_z,\quad t=\frac{R_p\eta_0}{\epsilon^2\sigma}\tilde{t},\quad \tau_d=\frac{\epsilon\sigma}{R_p}\tilde{\tau_d} \tag{21}$$

are employed to make the model equations dimensionless. Notice that the transformations for v_r and v_z also apply to U_t and V_{app}, respectively. Here, η_0 is the characteristic viscosity scale which is obtained by non-dimensionalizing the power-law given in Eq. (7):

$$\eta_0=m^{\frac{1}{n}}\left(\frac{\epsilon\sigma}{R_p}\right)^{1-\frac{1}{n}} \tag{22}$$

The dimensionless governing equations are written as:

$$\frac{1}{\tilde{r}}\frac{\partial}{\partial\tilde{r}}(\tilde{r}\tilde{v}_r)+\frac{\partial\tilde{v}_z}{\partial\tilde{z}}=0 \tag{23}$$

and

$$\frac{\partial\tilde{P}}{\partial\tilde{r}}=-\frac{\partial}{\partial\tilde{z}}\left[\left(-\frac{\partial\tilde{v}_r}{\partial\tilde{z}}\right)^n\right],\qquad \frac{\partial\tilde{P}}{\partial\tilde{z}}=0 \tag{24}$$

The interface conditions become

$$\tilde{v_r}=\tilde{U}_t \tag{25}$$

$$\tilde{v_z}-\frac{1}{2}\frac{\partial\tilde{h}}{\partial\tilde{r}}\tilde{v}_r=\frac{1}{2}\frac{\partial\tilde{h}}{\partial\tilde{t}} \tag{26}$$

and

$$\tilde{P}=2-\frac{1}{2\tilde{r}}\frac{\partial}{\partial\tilde{r}}\left(\tilde{r}\frac{\partial\tilde{h}}{\partial\tilde{r}}\right),\qquad -\tilde{\eta}\frac{\partial\tilde{v}_r}{\partial\tilde{z}}=\tilde{\tau_d} \tag{27}$$

where

$$\tilde{\eta}=\left|\frac{\partial\tilde{v}_r}{\partial\tilde{z}}\right|^{n-1} \tag{28}$$

Finally, the dimensionless boundary and initial conditions read:

$$\frac{\partial\tilde{h}}{\partial\tilde{t}}\Big|_{\tilde{r}_\infty}=-\tilde{V}_{app},\qquad \tilde{p}|_{\tilde{r}_\infty}=0\qquad \frac{\partial\tilde{h}}{\partial\tilde{r}}\Big|_{\tilde{r}=0}=0\qquad \frac{\partial\tilde{p}}{\partial\tilde{r}}\Big|_{\tilde{r}=0}=0 \tag{29}$$

and

$$\tilde{h}=\tilde{h}_{00}+\tilde{r}^2 \tag{30}$$

Solving the radial component of the equation of motion in Eq. (24) while employing the assumption of symmetry around the radial axis and the no-slip condition in Eq. (25), yields:

$$\tilde{v_r}=\tilde{U}_t+\frac{1}{\frac{1}{n}+1}\left(-\frac{\partial\tilde{P}}{\partial\tilde{r}}\right)^{1/n}\left[\left(\frac{\tilde{h}}{2}\right)^{\frac{1}{n}+1}-\tilde{z}^{\frac{1}{n}+1}\right] \tag{31}$$

Here, the first term gives rise to a plug-flow velocity profile while the second term results in a parabolic-like flow. By taking the derivative with respect to z of Eq. (31), the following expression for the tangential stress balance is obtained:

$$-\frac{\tilde{h}}{2}\frac{\partial\tilde{P}}{\partial\tilde{r}}=\tilde{\tau_d} \tag{32}$$

Inserting τ_d and Eq. (20) into the boundary integral equation given in Eq. (19), yields in dimensionless form:

$$\tilde{U}_t=-\frac{1}{2\pi\lambda^*}\int_0^{\tilde{r}_\infty}\int_0^{\pi}\frac{\tilde{h}}{2}\frac{\partial\tilde{P}}{\partial\tilde{r}}\frac{\cos\theta}{\sqrt{\tilde{r}^2+\tilde{\rho}^2-2\tilde{r}\tilde{\rho}\cos\theta}}\,\mathrm{d}\theta\,\mathrm{d}\tilde{\rho} \tag{33}$$

where λ^* is the dispersed to continuous viscosity ratio, given as: $\lambda^*=\frac{\epsilon\mu_d}{\eta_0}$.

Eq. (31) is then inserted into the continuity equation given in Eq. (23), which is solved for v_z. By inserting both v_r and v_z into the kinematic condition in Eq. (26), it can be manipulated to give the thinning equation:

$$\frac{\partial\tilde{h}}{\partial\tilde{t}}=-\frac{1}{\tilde{r}}\frac{\partial}{\partial\tilde{r}}\left[\tilde{r}\left(-\frac{\partial\tilde{P}}{\partial\tilde{r}}\right)^{1/n}\tilde{h}^{2n+1}\right]\frac{n}{(1+2n)2^{1/n+1}}-\frac{1}{\tilde{r}}\frac{\partial}{\partial\tilde{r}}(\tilde{r}\tilde{U}_t\tilde{h}) \tag{34}$$

Moreover, adding a term accounting for the attractive van der Waals forces, which is used to estimate the film rupture, to the normal stress balance in Eq. (27), the pressure equation is obtained:

$$\tilde{P}=2-\frac{1}{2\tilde{r}}\frac{\partial}{\partial\tilde{r}}\left(\tilde{r}\frac{\partial\tilde{h}}{\partial\tilde{r}}\right)+\frac{A^*}{\tilde{h}^3} \tag{35}$$

where A^* is the dimensionless Hamaker constant that is defined as $A^*=\frac{A}{6\pi\epsilon^6R_p^2\sigma}$.

The thinning, the pressure, and the boundary integral equations are solved simultaneously with the boundary conditions in Eq. (29), starting with the initial condition in Eq. (30). In this general case, the particle interfaces are considered partially mobile.

2.2.1. Immobile interfaces

When λ^* is very large, it can be seen from Eq. (33) that the contribution of the tangential velocity is negligible, thus the thinning equation reduces to:

$$\frac{\partial\tilde{h}}{\partial\tilde{t}}=-\frac{1}{\tilde{r}}\frac{\partial}{\partial\tilde{r}}\left[\tilde{r}\left(-\frac{\partial\tilde{P}}{\partial\tilde{r}}\right)^{1/n}\tilde{h}^{2n+1}\right]\frac{n}{(1+2n)2^{1/n+1}} \tag{36}$$

As the tangential velocity does not appear in the model when the interfaces are immobile, the boundary integral equation is omitted, and only the thinning and the pressure equations are solved.

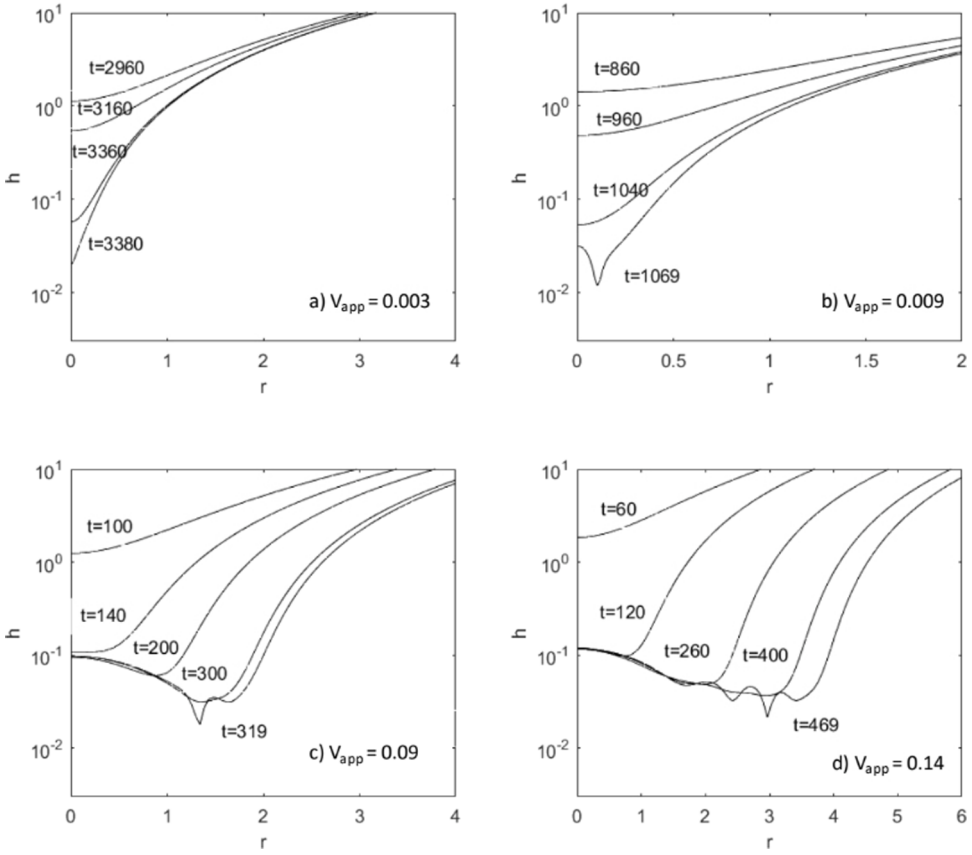

Fig. 2. Figure 5 of Ozan and Jakobsen (2019a) recreated to validate the non-Newtonian solver. Time development of film thickness as a function of r with $n = 1$ for different approach velocities. The profiles are obtained for immobile interfaces, $A^* = 10^{-4}$, $r_\infty = 15$ and $h_{00} = 10$.

2.2.2. Fully mobile interfaces

As λ^* approaches zero, the interfaces become fully mobile and the plug-flow term dominates the thinning equation:

$$\frac{\partial \tilde{h}}{\partial \tilde{t}} = -\frac{1}{\tilde{r}}\frac{\partial}{\partial \tilde{r}}(\tilde{r}\tilde{U}_t\tilde{h}) \tag{37}$$

Provided that λ^* is small enough to render the interfaces fully mobile, its effect on the drainage behavior disappears. By defining a new tangential velocity $\hat{U}_t$, the boundary integral equation can be rewritten as:

$$\hat{U}_t = \lambda^*\tilde{U}_t = -\frac{1}{2\pi}\int_0^{\tilde{r}_\infty}\int_0^{\pi}\frac{\tilde{h}}{2}\frac{\partial \tilde{P}}{\partial \tilde{r}}\frac{\cos\theta}{\sqrt{\tilde{r}+\tilde{\rho}-2\tilde{r}\tilde{\rho}\cos\theta}}\,\mathrm{d}\theta\,\mathrm{d}\tilde{\rho} \tag{38}$$

Then, by manipulating the transformation given for the time in Eq. (21) as

$$t = \frac{R_p\eta_0}{\epsilon^2\lambda^*\sigma}\tilde{t}_\lambda \tag{39}$$

the thinning equation for the fully mobile interfaces is found:

$$\frac{\partial \tilde{h}}{\partial \tilde{t}_\lambda} = -\frac{1}{\tilde{r}}\frac{\partial}{\partial \tilde{r}}(\tilde{r}\hat{U}_t\tilde{h}) \tag{40}$$

The new transformation applied for the fully mobile case also changes the first boundary condition in Eq. (29) into:

$$\frac{\partial \tilde{h}}{\partial \tilde{t}_\lambda}\Big|_{\tilde{r}_\infty} = -\lambda^*\tilde{V}_{app} \tag{41}$$

3. Results and discussion

The non-Newtonian drainage model obtained in Section 2 is solved for various degrees of interfacial mobility. The numerical procedure and the solver validation are presented in Section 3.1. The simulation results, then, are given and discussed in Section 3.2. The effect of the non-Newtonian behavior on the film drainage is examined through the film thickness, the excess pressure, the tangential stress and the viscosity profiles. Even though the drainage model cannot simulate the coalescence phenomena in full, it is possible to estimate the onset of coalescence, which is indicated by the rupture of the thin film. The time from the beginning of the drainage until the rupture is taken as the coalescence time, and presented as a function of the power-index, the relative approach velocity and the viscosity ratio. As all the variables are in dimensionless form, the tildes are excluded hereafter.

3.1. Numerical procedure and validation

The boundary integral, the thinning, and the pressure equations, respectively Eqs. (33)–(35) are solved simultaneously in the partially mobile case, and the boundary and initial conditions given in Eqs. 29 and 30 are employed. When the interfaces are immobile, Eq. (33) becomes redundant as the tangential mobility is zero, and Eq. (36) is used as the thinning equation. The fully mobile solver, on the other hand, employs Eqs. (40) and (41) together with the pressure equation as given in Eq. (35). In all solvers, the time derivatives discretized using a second order backward finite differentiation, and a Chebyshev-based spectral method is used in spatial discretization as described by Guo et al. (2013).

Although the boundary integral equation significantly decreases the computational costs by providing the tangential velocity at the interface without requiring the particle side flow fields to be solved, it has an inherent singularity that must be addressed. The methodology suggested by Ozan and Jakobsen (2019a) is followed for the treatment of this singularity, and the boundary integral equation is rewritten in discretized form as:

$$\hat{U}_t = \lambda^*\tilde{U}_t = [A_{int}]\tau_d \tag{42}$$

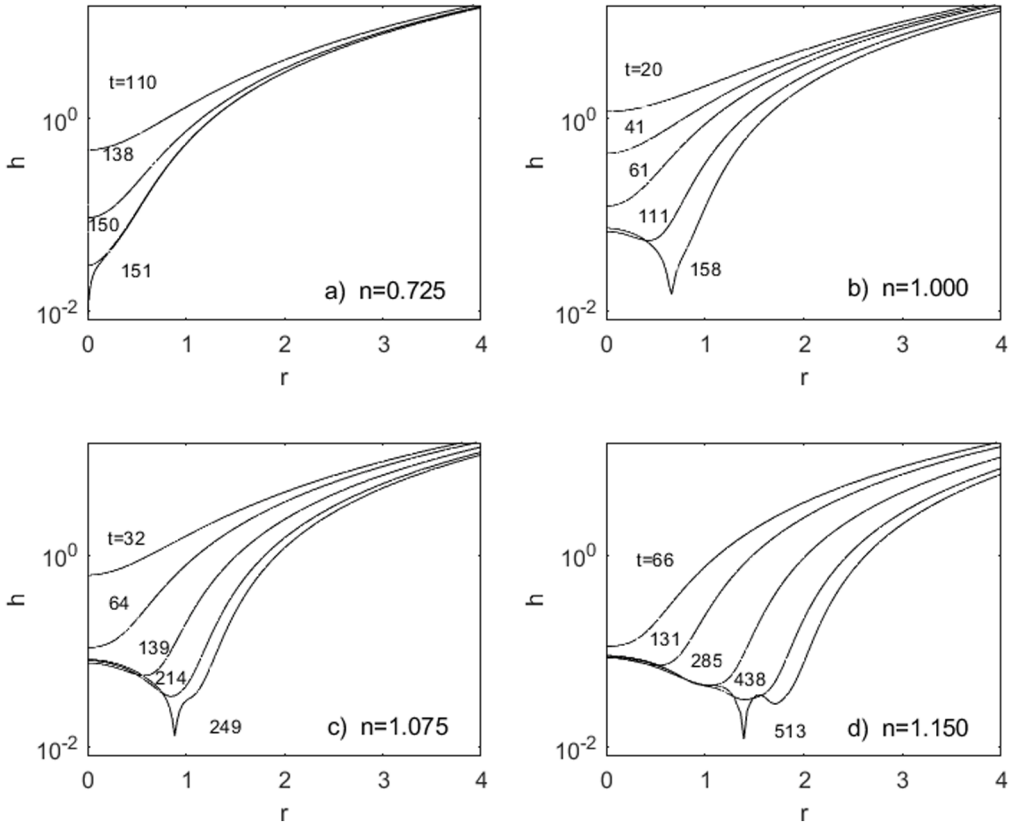

Fig. 3. Time development of film thickness as a function of r for immobile interfaces obtained with $V_{app} = 0.05$, $A^* = 10^{-4}$, $r_\infty = 30$ and $h_{00} = 2$.

where $[A_{int}]$ is a matrix that numerically carries out the double integration in Eqs. 33 and 38. Further description of the matrix can be found in Ozan and Jakobsen (2019a). To test the validity of the singularity treatment and the solvers, Fig. 5 of Ozan and Jakobsen (2019a) is reproduced, where the time evolution of the film thickness is presented for four different velocities by considering immobile interfaces. Their figure is recreated in Fig. 2 by setting $n = 1$ in the corresponding non-Newtonian solver. The results in Fig. 2 agree well with theirs.

A final comment should be made on the validity of the gentle collision assumption during the simulations. This assumption requires the deformed film radius to be much smaller than the particle radius. Thus, to ensure that this condition is satisfied, the largest radial rim position reached during the simulations is limited to $0.1 \sim 0.2$ of the computation domain size r_∞.

3.2. Non-Newtonian film drainage

In Fig. 3, the time evolution of the film thickness for different values of the power index n is given at a constant value of V_{app}. The three different drainage regimes Ozan and Jakobsen (2019a) detected while investigating the effect of V_{app}, are also present in Fig. 3. In their work, the transitions between these regimes were found to occur with V_{app}. In the current work, it is seen that these transitions can also stem from the value of n. Fig. 3(a), where $n = 0.725$, displays the low-velocity regime. In this regime, the film ruptures from the center of the fluid particle interface, i.e., at $r = 0$, which is called nose rupture. This type of rupture happens when the attractive van der Waals forces become significant before the capillary forces can act substantially and change the interfaces' shape visibly. Increasing the power index to 1.000 yields case (b). Here, a dimple shape can be observed, meaning that the dimpled drainage regime is reached. The formation of a dimple also implies that the capillary forces are now more significant compared to the case in Fig. 3(a). This can be explained through the effect of n on the viscosity. As n increases, for similar magnitudes of shear rate, the viscosity is expected to increase, which can be associated with a decrease in the drainage rate. Then, the critical film thickness at which the intermolecular forces act significantly and result in film rupture, is reached in a longer time. Notice that this thickness is governed by the value of A^* only. As the collision is a constant velocity one, this results in the pressure in the film to build up continuously for longer time as well. In response to the pressure build-up, the interfaces deform to a larger radial extent and even start supporting rim structures. Further increasing n to 1.075 results in the emergence of a secondary rim to the right of the main rim as seen in Fig. 3(c), indicating the onset of the multiple rim drainage regime. Finally, for even higher n, as presented in Fig. 3(d), multiple local maxima and minima in the film thickness profiles can be observed right before the film rupture. As n increases, the radial position at which rupture occurs moves further away from $r = 0$. Also, the estimated coalescence time increases due to the rim formation, which tends to delay the film drainage.

Fig. 4 presents the time development of the excess pressure profiles in the film corresponding to the film thicknesses in Fig. 3. Regardless of the value of n or the type of the interfacial deformations, in all results, the excess pressure in the film builds up with time. For case (a), where a nose rupture occurs, the excess pressure attains a maximum always at $r = 0$, which eventually shows an asymptotic trend as the film ruptures. In the other cases, the excess pressure also builds up more at the center during the early stages of the drainage. However, after some time, the maximum shifts to the position of the rim, as can be seen by comparing Figs. 3 and 4. Upon reaching the final time step before the film ruptures, a sharp peak is observed for each case. This peak occurs due to the attractive intermolecular forces, which dominate the pressure profile around the rims where the film thickness is the smallest. In Fig. 4(d), a local maximum is detectable in the last excess pressure profile corresponding to the secondary rim visible in Fig. 3(d).

The time evolution of the particle side tangential stress (Eq. (32)) and the corresponding viscosity profiles evaluated at the interface are

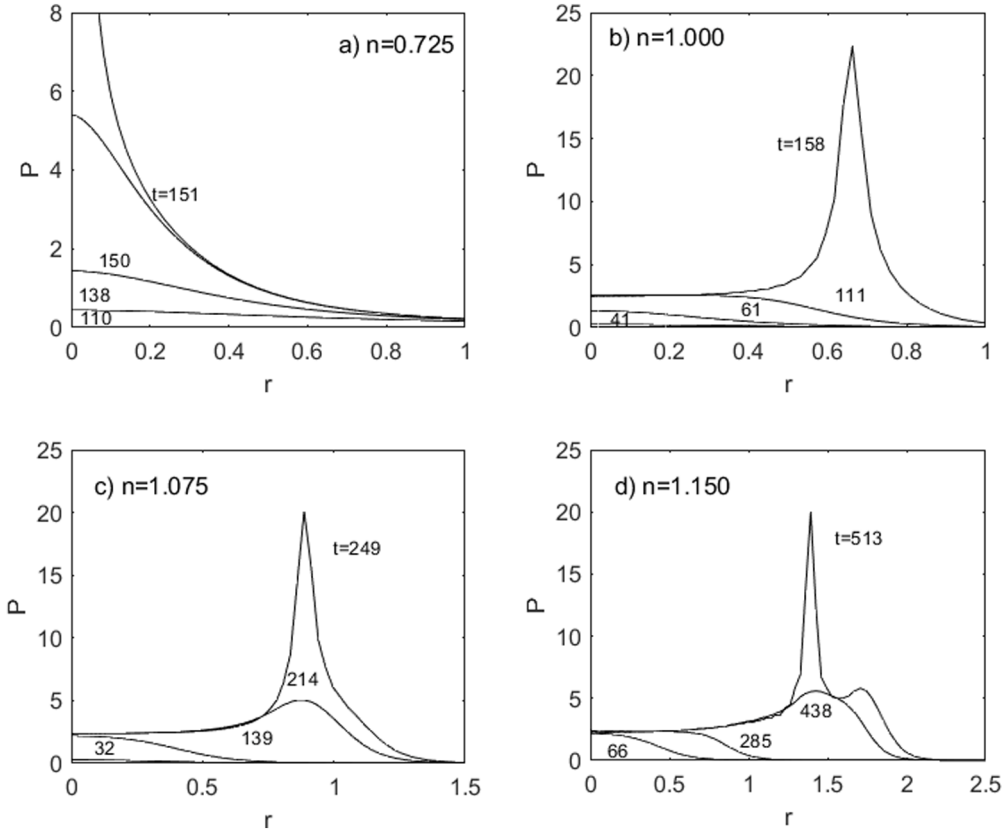

Fig. 4. Time development of excess pressure as a function of r for partially mobile interfaces obtained with λ^* $V_{app} = 0.05$, $A^* = 10^{-4}$, $r_\infty = 30$ and $h_{00} = 2$.

given in Fig. 5, for a shear-thinning film with $n = 0.9$ and for a shear-thickening film with $n = 1.1$. In Fig. 5(a), the tangential stress profiles form a maximum that increases with time, whereas the corresponding viscosity profiles in Fig. 5(b), form a more and more evident minimum with time, whose position is the same as the location of the maximum τ_d. The opposite trend is observed for the shear-thickening fluid in Figs. 5(c) and (d). Here, the tangential stress maxima coincide with viscosity's maxima. Just as the excess pressure build-up, the increase in the tangential stress is also a result of the interfacial deformations, and the maximum of τ_d closely follows the rim position. Then, since this position coincides with the minimum and the maximum of η respectively for the shear-thinning and the shear-thickening case, the resistance to the film drainage around the rim is the lowest for shear-thinning films and the largest for shear-thickening ones. In other words, a rim can more easily travel in the positive r direction when the film is shear-thinning.

The maximum tangential velocity is presented as a function of time for different values of n in Fig. 6. This value can be taken as an indicator of the tangential mobility of the interface, which is of key importance in coalescence studies. In the early stages of the drainage process, from $t = 0$ to about $t \approx 25$ for the particular parameter set, the maximum tangential velocity (thus the mobility of the interface) is larger for lower values of n. As n indicates how viscous the film is, for a given shear rate, when it is low, the drainage is easier, and the interfaces are more mobile. After this stage, some crossover is seen between the different curves, as the extent of the interfacial deformations at a given time is different for different n. Then, the asymptotic incline at the end of each curve indicates the rupture of the film. The results show that the fluid particles coalesce more quickly when n is lower, as the drainage rate is faster.

Although not presented here explicitly, the simulations with finite values of λ^* indicate that the observations obtained by considering immobile interfaces are also valid when the interfaces are fully or partially mobile. In other words, regardless of the extent of the tangential mobility, the power index n affects the system in the same way, and the same three types of interfacial deformations/drainage regimes are encountered.

Fig. 7 presents the coalescence time, t_c, as a function of V_{app} and n for $\lambda^* = 10$, where the interfaces are partially mobile in each data-set. For all n values investigated in Fig. 7, three drainage regimes can be identified. At low velocities, the relation between $\log(t_c)$ and $\log(V_{app})$ decreases linearly. In this region, the t_c curves for different power index values lay approximately on the same line, showing that the non-Newtonian behavior is not significantly influential on the drainage in the low-velocity regime. The transition to the dimpled drainage regime occurs when the t_c curves start to deviate from the linear trend. Note that the higher the value of n, the earlier the transition occurs, as larger n implies a stronger resistance to the flow within the film, which enables the capillary forces to act more significantly before the rupture and results in rim formation. Within this regime, the t_c curves begin to separate, indicating that the non-Newtonian behavior of the film starts influencing the drainage behavior and the estimated coalescence time. Once this regime is reached, t_c increases with n, implying that coalescence becomes easier as the film gets more shear-thinning. This is in agreement with the conclusions of Fan et al. (2020) from their experiments, where the coalescence efficiency was found to be larger for higher CMC-concentrations, i.e., for lower n. The coalescence time, then, at a larger V_{app} passes through a minimum and starts increasing with V_{app}, which is associated with the emergence of additional rims at the interface. Thus, the multiple-rim drainage regime is reached. The increasing t_c trend seen in this regime was not observed in experiments when it was first suggested by Ozan and Jakobsen (2019a). In a recent study, however, Aarøen et al. (2021) encountered the same trend for high approach velocities in their experiments with oil-in-water emulsions. As, in this regime, the separations between the t_c curves grow

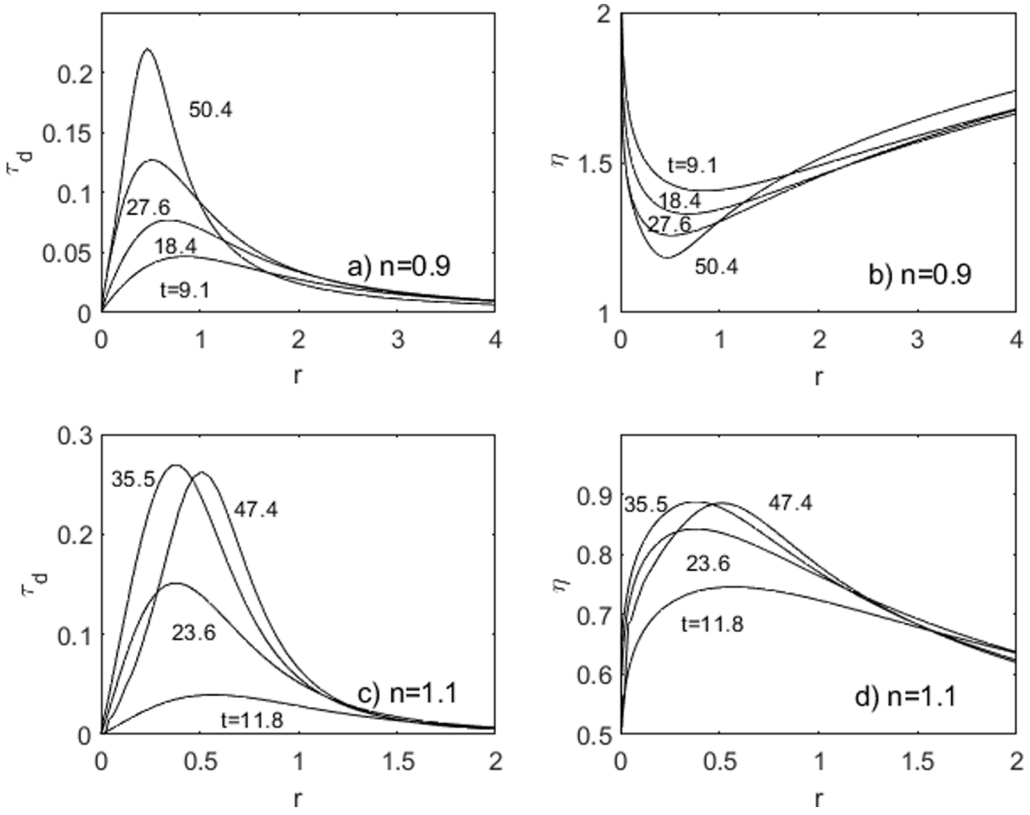

Fig. 5. Time evolution of the particle side tangential stress and viscosity evaluated at the interface. The profiles are obtained with $V_{app} = 0.09$, $A^* = 10^{-4}$, $r_\infty = 30$ and $h_{00} = 2$.

even larger, the effect of the power index is more prominent. Overall, the impact of the non-Newtonian film behavior on the film drainage amplifies with the approach velocity. As with the transitions into the dimpled drainage regime, the transitions into the multiple-rim regime occur at lower velocities for larger values of n.

Fig. 8 shows the coalescence time, t_c, as a function of the dispersed to continuous phase viscosity ratio, λ^*, for different values of n. The results are obtained by considering partially mobile interfaces, i.e. the thinning equation is solved without any further simplifications as given in Eq. (34). These results are then combined with the ones obtained for the fully mobile and the immobile cases for the lower and upper limits of λ^*, respectively. It can be observed that the effect of the power index is very prominent in the high λ^* limit, where the interfaces are tangentially immobile. As λ^* decreases, the effect of n diminishes and eventually completely disappears for λ^* values that are low enough to render the interfaces fully mobile. Fig. 8 reveals that the interfaces are fully mobile when $\lambda^* \leq 0.1$ for all n, while the λ^*-limit after which the interfaces are completely immobilized seem to increase with n, e.g. 10^3 for $n = 0.8$ and 10^5 for $n = 1.1$.

The Hamaker constant, A^*, decreases the coalescence time for the Newtonian films, as can be seen in Fig. 4 of Ozan and Jakobsen (2019a). It is found to affect the system in the same way for the shear-thinning and the shear-thickening films as well, even though the results are not presented here. Since the critical film rupture thickness increases with A^*, the coalescence occurs at a larger minimum film thickness, resulting in lower t_c.

4. Conclusions

In this work, the drainage of a thin non-Newtonian film bounded by two fluid particles is analyzed. The non-Newtonian continuous phase is taken as a generalized Newtonian fluid, i.e., only viscous, obeying the power-law. The effect of the power-index n, thus of the non-Newtonian behavior itself, on the drainage behavior and the coalescence time

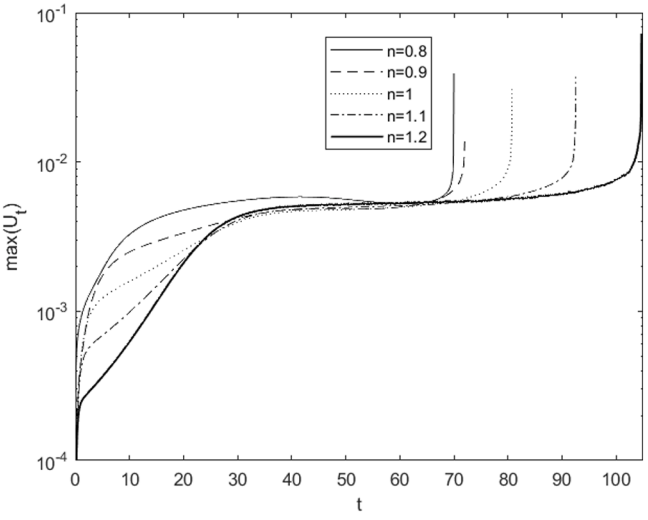

Fig. 6. The maximum value of the tangential velocity of the interface as a function of time for different values of n. All results are obtained with $\lambda^* = 10$, $A^* = 10^{-4}$, $h_{00} = 2$ and $r_\infty = 30$.

t_c is investigated. The results revealed no dimple formation during the drainage for low enough values of n. Increasing the power-index to larger values first results in a single rim formation, i.e., dimple formation, and then causes multiple rim structures to appear at the interfaces. It is also seen that the rims can travel further in the radial direction when n is smaller, as the viscosity attains its lowest value around the rim for shear-thinning fluids. When the interfaces are not deformed enough to exhibit rim formation (typically at low V_{app}), the non-Newtonian behavior is found to have only a negligible impact on

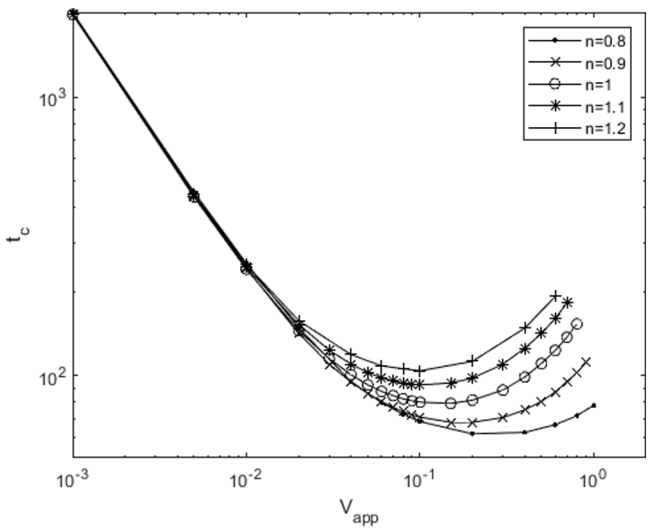

Fig. 7. Coalescence time as a function of relative approach velocity for varying n-values with $A^* = 10^{-4}$, $r_\infty = 30$, $\lambda^* = 10$ and $h_{00} = 2$.

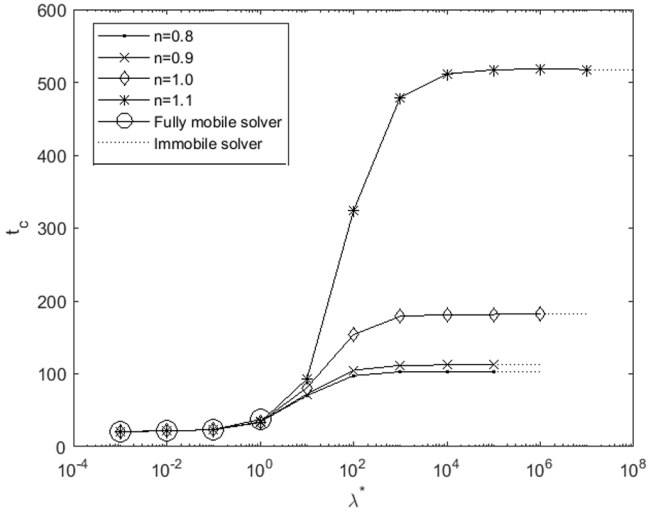

Fig. 8. Coalescence time as a function of dispersed to continuous phase viscosity ratio for varying values of the power index with $A^* = 10^{-4}$, $V_{app} = 0.09$, $h_{00} = 2$ and $r_\infty = 30$.

t_c. As the rims begin to emerge with increasing V_{app} on the other hand, the coalescence time is affected by the value of n considerably. At a given V_{app}, the drainage rate slows down with n, and consequently t_c increases. The extent of this increase in t_c is found to scale with the value of V_{app}. Finally, t_c is affected by the non-Newtonian behavior the most when the interfaces are immobile. As the tangential mobility increases, the gap between the t_c values for different n narrows down and eventually vanishes when the fully mobile limit is reached.

CRediT authorship contribution statement

Maria Fanebust: Conceptualization, Methodology, Software, Validation, Formal analysis, Investigation, Writing – original draft, Writing – review & editing. **Suat Canberk Ozan:** Conceptualization, Methodology, Software, Validation, Formal analysis, Investigation, Writing – original draft, Writing – review & editing, Visualization, Supervision, Project administration. **Hugo Atle Jakobsen:** Conceptualization, Resources, Supervision, Project administration, Funding acquisition.

Declaration of competing interest

The authors declare that they have no known competing financial interests or personal relationships that could have appeared to influence the work reported in this paper.

Acknowledgments

The work was supported by the Research Council of Norway (Grant no. 267669).

References

Aarøen, O., Riccardi, E., Sletmoen, M., 2021. Exploring the effects of approach velocity on depletion force and coalescence in oil-in-water emulsions. RSC Adv. 11 (15), 8730–8740.
Abid, S., Chesters, A., 1994. The drainage and rupture of partially-mobile films between colliding drops at constant approach velocity. Int. J. Multiph. Flow. 20 (3), 613–629.
Acharya, A., Mashelkar, R., Ulbrecht, J.J., 1978. Bubble formation in non-Newtonian liquids. Ind. Eng. Chem. Fundam. 17 (3), 230–232.
Al-Matroushi, E., Borhan, A., 2009. Coalescence of drops and bubbles rising through a non-Newtonian fluid in a tube. Ann. New York Acad. Sci. 1161 (1), 225–233.
Bazhlekov, I., Chesters, A., Van de Vosse, F., 2000. The effect of the dispersed to continuous-phase viscosity ratio on film drainage between interacting drops. Int. J. Multiph. Flow. 26 (3), 445–466.
Chan, D.Y., Klaseboer, E., Manica, R., 2011. Film drainage and coalescence between deformable drops and bubbles. Soft Matter 7 (6), 2235–2264.
Chesters, A., 1991. Modelling of coalescence processes in fluid-liquid dispersions: a review of current understanding. Chem. Eng. Res. Des. 69 (A4), 259–270.
Coulaloglou, C., 1975. Dispersed phase interactions in an agitated flow vessel. (Ph.D. thesis, Ph. D. Dissertation). Illinois Institute of Technology, Chicago.
Davis, R.H., Schonberg, J.A., Rallison, J.M., 1989. The lubrication force between two viscous drops. Phys. Fluids A 1 (1), 77–81.
Dekee, D., Carreau, P., Mordarski, J., 1986. Bubble velocity and coalescence in viscoelastic liquids. Chem. Eng. Sci. 41 (9), 2273–2283.
Derjaguin, B., Kussakov, M., 1939. Anomalous properties of thin polymolecular films. Acta Phys. URSS 10 (1), 25–44.
Fan, W., Du, M., Sun, Y., Chen, H., 2020. Coalescence characteristics of side-by-side growing bubbles in carboxymethyl cellulose solutions. Chem. Eng. Technol. 43 (2), 230–239.
Guo, W., Labrosse, G., Narayanan, R., 2013. The Application of the Chebyshev-Spectral Method in Transport Phenomena. Springer Science & Business Media.
Klaseboer, E., Chevaillier, J.P., Gourdon, C., Masbernat, O., 2000. Film drainage between colliding drops at constant approach velocity: experiments and modeling. J. Colloid Interface Sci. 229 (1), 274–285.
Li, H.Z., 1999. Bubbles in non-Newtonian fluids: Formation, interactions and coalescence. Chem. Eng. Sci. 54 (13–14), 2247–2254.
Li, H.Z., Frank, X., Funfschilling, D., Mouline, Y., 2001. Towards the understanding of bubble interactions and coalescence in non-Newtonian fluids: a cognitive approach. Chem. Eng. Sci. 56 (21–22), 6419–6425.
Li, H., Mouline, Y., Choplin, L., Midoux, N., 1997. Chaotic bubble coalescence in non-Newtonian fluids. Int. J. Multiph. Flow. 23 (4), 713–723.
Liao, Y., Lucas, D., 2010. A literature review on mechanisms and models for the coalescence process of fluid particles. Chem. Eng. Sci. 65 (10), 2851–2864.
Lin, T.-J., Lin, G.-M., 2009. Mechanisms of in-line coalescence of two-unequal bubbles in a non-Newtonian fluid. Chem. Eng. J. 155 (3), 750–756.
Ozan, S.C., Hosen, H.F., Jakobsen, H.A., 2021. On the prediction of coalescence and rebound of fluid particles: A film drainage study. Int. J. Multiph. Flow. 135, 103521.
Ozan, S.C., Jakobsen, H.A., 2019a. On the effect of the approach velocity on the coalescence of fluid particles. Int. J. Multiph. Flow. 119, 223–236.
Ozan, S.C., Jakobsen, H.A., 2019b. On the role of the surface rheology in film drainage between fluid particles. Int. J. Multiph. Flow. 120, 103103.
Ozan, S.C., Jakobsen, H.A., 2020. Effect of surface viscoelasticity on the film drainage and the interfacial mobility. Int. J. Multiph. Flow. 130, 103377.
Shinnar, R., Church, J.M., 1960. Statistical theories of turbulence in predicting particle size in agitated dispersions. Indus. Eng. Chem. 52 (3), 253–256.
Sun, W., Zhu, C., Fu, T., Yang, H., Ma, Y., Li, H., 2017. The minimum in-line coalescence height of bubbles in non-Newtonian fluid. Int. J. Multiph. Flow. 92, 161–170.
Yiantsios, S.G., Davis, R.H., 1991. Close approach and deformation of two viscous drops due to gravity and van der waals forces. J. Colloid Interface Sci. 144 (2), 412–433.
Zhu, C., Li, S., Fu, T., Ma, Y., 2018. Velocity evolution for the coalescence of two in-line bubbles rising in non-Newtonian fluids. Theor. Found. Chem. Eng. 52 (3), 459–464.